



# AMERICAN METEOROLOGICAL SOCIETY

*Journal of Climate*

## **EARLY ONLINE RELEASE**

This is a preliminary PDF of the author-produced manuscript that has been peer-reviewed and accepted for publication. Since it is being posted so soon after acceptance, it has not yet been copyedited, formatted, or processed by AMS Publications. This preliminary version of the manuscript may be downloaded, distributed, and cited, but please be aware that there will be visual differences and possibly some content differences between this version and the final published version.

The DOI for this manuscript is doi: 10.1175/JCLI-D-15-0564.1

The final published version of this manuscript will replace the preliminary version at the above DOI once it is available.

If you would like to cite this EOR in a separate work, please use the following full citation:

Bodas-Salcedo, A., P. Hill, K. Furtado, K. Williams, P. Field, J. Manners, P. Hyder, and S. Kato, 2016: Large contribution of supercooled liquid clouds to the solar radiation budget of the Southern Ocean. *J. Climate*. doi:10.1175/JCLI-D-15-0564.1, in press.

© 2016 American Meteorological Society



1           **Large contribution of supercooled liquid clouds to the solar**  
2                           **radiation budget of the Southern Ocean**

3    A. BODAS-SALCEDO \* , P. G. HILL, K. FURTADO, K. D. WILLIAMS,  
          P. R. FIELD, J. C. MANNERS, P. HYDER,

*Met Office Hadley Centre, Exeter, United Kingdom*

4                           S. KATO

*NASA Langley Research Center, Hampton, Virginia, USA*

*\*Corresponding author address: A. Bodas-Salcedo, Met Office Hadley Centre, FitzRoy Road, Exeter,  
EX1 3PB, United Kingdom.*

*E-mail: alejandro.bodas@metoffice.gov.uk*

## ABSTRACT

5  
6 The Southern ocean is a critical region for global climate, yet large cloud and solar radiation  
7 biases over the Southern Ocean are a long-standing problem in climate models and are  
8 poorly understood, leading to biases in simulated sea-surface-temperatures. In this study  
9 we show that supercooled liquid clouds are central to understanding and simulating the  
10 Southern Ocean environment. We use a combination of satellite observational data and  
11 detailed radiative transfer calculations to quantify the impact of cloud phase and cloud  
12 vertical structure on the reflected solar radiation in the southern hemisphere summer. We  
13 find that clouds with supercooled liquid tops dominate the population of liquid clouds. The  
14 observations show that clouds with supercooled liquid tops contribute between 27% and  
15 38% to the total reflected solar radiation between 40°S and 70°S, and climate models are  
16 found to poorly simulate these clouds. Our results quantify the importance of supercooled  
17 liquid clouds in the Southern Ocean environment, and highlight the need to improve our  
18 understanding of the physical processes that control these clouds in order to improve their  
19 simulation in numerical models. This is not only important for improving the simulation of  
20 present-day climate and climate variability, but also relevant for increasing our confidence  
21 in climate feedback processes and future climate projections.

# 22 1. Introduction

23 Clouds are major controllers of the top of the Atmosphere (TOA) and surface energy  
24 budgets, and therefore play a leading role in determining the air-surface interaction that  
25 controls the evolution of important climate variables (Gregory and Morris 1996; Bennartz  
26 et al. 2013). Large solar radiation biases present in climate models over the Southern Ocean  
27 are largely associated with a poor simulation of low- and mid-level clouds (Williams et al.  
28 2013; Bodas-Salcedo et al. 2012, 2014). They may also affect tropical atmospheric circu-  
29 lations and precipitation patterns (Ceppi et al. 2012; Hwang and Frierson 2013). Recent  
30 observational studies show the prevalence of supercooled liquid water ( $T < 273.15\text{K}$ ) in low-  
31 level clouds in the mid-latitude oceans (Hu et al. 2010; Huang et al. 2012), but their simula-  
32 tion in climate models is still challenging (Cesana et al. 2012; Forbes and Ahlgrimm 2014).  
33 Their impact on the Earth’s radiation budget, although potentially significant (Hogan et al.  
34 2003), is poorly understood over large regions and has not been quantified. In addition to  
35 their importance for present-day simulations, cloud-phase radiative feedbacks also dominate  
36 the cloud changes in the high latitudes (Senior and Mitchell 1993; Tsushima et al. 2006).  
37 The effect of these clouds on the radiative biases detected in climate models can be better  
38 understood by quantifying their contribution to the radiation budget.

39 Bodas-Salcedo et al. (2014) analyse the shortwave reflected radiation model errors ac-  
40 cording to cloud regimes. The cloud regimes are defined using the cloud clustering algorithm  
41 developed by Williams and Webb (2009), applied to model data from the Coupled Model  
42 Intercomparison Project phase 5 (CMIP5, Taylor et al. 2012) and observations from the  
43 International Satellite Cloud Climatology Project (Rossow and Schiffer 1999, ISCCP). Using  
44 additional information from the Cloud-Aerosol Lidar and Infrared Pathfinder Satellite Obser-  
45 vations (CALIPSO) satellite (Winker et al. 2009), they show that the ISCCP cloud clusters  
46 contain large internal variability in cloud vertical structure. This is particularly acute for  
47 the so-called mid-level cloud regime, which is the cloud cluster that contributes more to  
48 the model biases. One of the aims of this study is to provide a more direct connection be-

49 tween cloud vertical structure and reflected shortwave radiation. Given the recently-observed  
50 prevalence of supercooled liquid water over the Southern Ocean, and the fact that cloud mi-  
51 crophysical processes are especially challenging to models, a second aim is to quantify the  
52 contributions of cloud phase to the shortwave radiation budget.

53 Our ability to observe the vertical structure of clouds has been greatly enhanced in  
54 the last decade with the availability of two active instruments, CloudSat and CALIPSO  
55 satellites, flying in formation as part of the A-Train (Stephens et al. 2002). These instruments  
56 have been recently used to estimate the climatological impact of clouds on the atmospheric  
57 radiative heating (L’Ecuyer et al. 2008; Haynes et al. 2013). Here we use satellite data and  
58 radiative transfer simulations to quantify the contributions of different cloud types and cloud  
59 thermodynamic phase to the TOA radiation budget. We also analyse data from the most  
60 recent multi-model ensemble simulations to understand the implications of the present-day  
61 biases observed in the current generation of models over the Southern Ocean. We restrict  
62 our analysis to the Austral Summer season as our main focus in this study is in the solar  
63 part of the spectrum.

64 The paper is structured as follows. Section 2 describes the satellite data, radiative trans-  
65 fer calculations, the model simulations, and the cyclone compositing methodology. This  
66 section also considers the implications of the uncertainty in the cloud top phase identifica-  
67 tion. Section 3 presents the main results of the study, and Section 4 summarises the main  
68 conclusions and discusses future work.

## 69 **2. Data and methodology**

### 70 *a. Satellite Data*

71 The combined CERES/CloudSat/CALIPSO/MODIS (CCCM) dataset (Kato et al. 2010,  
72 2011) provides information on the vertical occurrence of clouds and their radiative proper-  
73 ties. The Clouds and the Earth’s Radiant Energy System (CERES) instruments measure

74 the solar reflected and thermally emitted radiances at the top of the Atmosphere. Fluxes  
75 are then obtained by applying an empirical angular distribution model (Loeb et al. 2005).  
76 Although the CERES fluxes are not direct measurements, we still use this terminology to  
77 distinguish between the CERES estimates and the fluxes obtained from radiative transfer  
78 calculations. The CERES radiometers have a horizontal resolution of 20 km at nadir. Two  
79 CERES instruments fly onboard the Aqua satellite, in tight formation with CloudSat and the  
80 CALIPSO satellites, as part of the A-Train (Stephens et al. 2002). The Moderate Resolution  
81 Imaging Spectroradiometer (MODIS) is also onboard the Aqua satellite. These four instru-  
82 ments observe the same scene within a few tens of seconds difference. The Cloud Profiling  
83 Radar (CPR) onboard CloudSat and the Cloud-Aerosol Lidar with Orthogonal Polarization  
84 (CALIOP) onboard CALIPSO provide information on the vertical distribution of clouds,  
85 and MODIS gives information on vertically-integrated properties. Data from these three  
86 instruments are used to provide cloud radiative properties and thermodynamic phase. The  
87 CCCM dataset co-locates information from these three instruments with radiation measure-  
88 ments from the CERES instrument. The number of cloud profiles in a CERES footprint  
89 can be as many as 50. For each CERES footprint (instrument with the coarsest resolution),  
90 CCCM defines up to sixteen 'cloud groups'. A cloud group is a set of vertical profiles within a  
91 CERES footprint that share the same vertical distribution of clouds, i.e. that have the same  
92 cloud boundary heights. They can be single radar-lidar columns, but they are generally not.  
93 It is a way of reducing data volumes without losing too much spatial variability information  
94 within the CERES field of view (FOV). When the number of unique cloud groups exceeds 16,  
95 profiles with nearly the same cloud top and base heights are combined. The vertical profile  
96 grouping process is detailed in Kato et al. (2010). For each of these cloud groups, cloud  
97 properties are reported with an approximate vertical resolution of 240 m. We use Release  
98 B1 of the CCCM dataset, and Table 1 provides a list of the variables that are used in this  
99 study. We also use the 2000-2013 climatology of TOA radiative fluxes from the CERES  
100 Energy Balanced and Filled (EBAF) Ed2.8 dataset for comparisons with model simulations

101 (Loeb et al. 2009).

102 Vertical profiles of cloud liquid and ice water contents (IWC, LWC, variables CCCM-  
103 85/86) are derived in six steps. For each cloud group of which cloud top and base heights  
104 are derived from CALIPSO and CloudSat, CCCM assigns a vertically constant extinction  
105 coefficient computed from the MODIS-derived cloud optical thickness, particle size, and  
106 phase for all overlapping layers. If CloudSat derived IWC or LWC is available, CCCM com-  
107 putes extinction coefficients due to ice particles or water particles for each cloud layer using  
108 CloudSat-derived cloud properties, and selects the one that gives a larger optical thickness  
109 for that layer. If CALIPSO-derived extinction is available, the extinction coefficient derived  
110 from MODIS or CloudSat is replaced by that derived from CALIPSO. Since CALIPSO is at-  
111 tenuated rapidly by water clouds, if the CALIPSO extinction profile is available, then CCCM  
112 assumes that the cloud is in the ice phase. CCCM integrates extinction coefficients vertically  
113 for each cloud group and normalize the total scaled optical thickness by the MODIS-derived  
114 scaled optical thickness. The scaled optical thickness is defined as  $(1 - g)\tau$ , where  $g$  is  
115 the asymmetry parameter and  $\tau$  is the cloud optical thickness. Therefore, the scaled optical  
116 thickness for cloud groups is equal to the corresponding scaled optical thickness derived from  
117 MODIS. CCCM converts the extinction coefficient back to IWC and LWC vertical profiles for  
118 each cloud group, and averages them from all cloud groups, weighted by their cloud fractions  
119 within each CERES footprint. For this calculation, the CALIPSO or CloudSat estimates  
120 of effective radius are used if available. If not, MODIS effective radius is used, assuming  
121 a constant particle size for the entire column. In summary, CALIPSO extinction profile is  
122 used if available, then CloudSat water contents if CALIPSO extinction is not available, and  
123 MODIS if neither CALIPSO nor CloudSat profiles are available. CCCM ice and liquid water  
124 paths, used for comparison with models in Section 3, are calculated by vertically integrating  
125 the CCCM LWC and IWC.

126 *b. Radiative transfer calculations*

127 CCCM does not provide radiative fluxes for individual cloud groups, so we run the  
128 Edwards-Slingo (Edwards and Slingo 1996) radiative transfer code on each vertical profile  
129 that describes a CCCM cloud group. For each CERES footprint, a clear-sky calculation is  
130 also performed. We perform these calculations for 5 Austral summers (December, January,  
131 February), from December 2006 to February 2011. Data for January 2011 are not available  
132 due to bad geolocation of CloudSat data, so a total of 420 days are processed. The cal-  
133 culations are restricted to the region between 40°S and 72.5°S. The radiative transfer code  
134 requires profiles of pressure, temperature, water vapour, ozone, cloud water contents (liquid  
135 and ice), and cloud particles effective dimensions (liquid and ice). CCCM provides cloud  
136 extinction (CCCM-84) and cloud liquid and ice water contents for each level (CCCM-85/86),  
137 averaged over all the cloud groups. We calculate the cloud droplet effective radius as

$$R_e = \frac{3}{2}CWC\rho^{-1}\beta^{-1},$$

138 where CWC,  $\rho$  and  $\beta$  are the condensate (liquid/ice) water content, density, and ex-  
139 tinction coefficient, respectively. Both phases can co-exist in the same cloud group, with  
140 independent optical properties. The effective radius is limited to a range between 4 and 30  
141 microns for liquid and 5 and 150 microns for ice. We use the same values of water con-  
142 tents and effective radius at each level for all cloud groups. This assumption effectively  
143 neglects the spatial variability in cloud properties in each layer. CCCM also provides in-  
144 formation on the vertical profile of temperature (CCCM-77), pressure (CCCM-76), water  
145 vapour (CCCM-78) and ozone (CCCM-79), which come from the NASA Global Modeling  
146 and Assimilation Office (GMAO) Goddard Earth Observing System version 4 (GEOS-4)  
147 reanalysis before November 2007, and G5-CERES after that (Bloom et al. 2005; Rienecker  
148 et al. 2008). Surface broadband albedo is also required as input (SSF-50).

149 CCCM also reports the fraction of the CERES footprint that is occupied by each cloud



150 group (CCCM-12). We use the independent pixel approximation to obtain an estimate  
151 of the radiative fluxes at CERES resolution by weighting each cloud group and clear-sky  
152 radiative transfer calculation by its area fraction. We compare these estimates with the  
153 CERES measurements of the reflected solar radiation (SSF-38) to evaluate the accuracy of  
154 the methodology. The calculations are virtually unbiased, and the frequency distribution of  
155 the estimated fluxes compares well with the observed distribution (Figure 1a), with some  
156 discrepancies in the low- and high-value ranges. The density plot in Figure 1b reinforces  
157 the conclusion that the radiative transfer calculations perform reasonably well across the  
158 entire range of scenes. Large differences are observed in those CERES footprints with the  
159 largest fluxes (greater than  $550 \text{ W m}^{-2}$ ), which correspond to thick clouds that tend to  
160 have glaciated tops. We have tested the impact of using different parametrisations of the  
161 ice optical properties that reduce the histogram differences for large values of reflected solar  
162 radiation. We use the parameterisation by Kristjansson et al. (1999) in our standard cal-  
163 culations (Figures 1a-b). This is the parameterisation used in the Met Office model at the  
164 time of writing. Figures 1c-d show the impact of replacing this standard parameterisation  
165 with a newer parameterisation (Baran et al. 2013). This newer parameterisation reduces the  
166 biases, but the results and conclusions of this study are robust to the choice of ice optical  
167 properties parameterisation.

168 The calculations overestimate the reflected solar radiation for dark scenes (i.e. clear-  
169 skies or very thin clouds). Several causes may contribute to this bias: inaccurate surface  
170 albedo (SSF-50), wrong amount of shortwave absorbers or the parameterisation of their  
171 radiative properties, or errors in scene identification (e.g. cloud fraction). The surface effect  
172 is taken into account in the radiative transfer calculations through the surface albedo. Apart  
173 from ocean, other two surface types have a significant population in the domain: permanent  
174 snow/ice and sea ice. Our calculations of TOA reflected fluxes are biased low over permanent  
175 snow, and biased high over sea ice. However, the population of these two surface is sufficiently  
176 small that the results shown in Figure 1 are dominated by the ocean points.

177 The Southern Ocean is a region dominated by strong winds, which affect the surface  
178 albedo. We have also tested the sensitivity of our radiative transfer calculations to the surface  
179 wind speed. We have split the population in two halves according to wind speed, and both  
180 halves show very similar biases (not shown). We therefore conclude that the dependency of  
181 surface albedo with wind speed does not play a significant role in our analysis.

182 We have also investigated the causes of the differences in the range between 400-600  $\text{W m}^{-2}$   
183 . They are substantially reduced if CERES FOVs with total number of good CALIPSO  
184 profiles (CCCM-11) less than 50 are discarded. CERES FOVs with a small number of  
185 good CALIPSO profiles may introduce a low bias in cloud fraction that makes the radiative  
186 transfer calculations to be biased low. It is clear that errors in the cloud identification can  
187 introduce large errors in the radiative transfer simulations. CALIOP plays a central role in  
188 the identification and retrieval of cloud properties. When CALIOP is not operational, the  
189 CCCM products rely on CloudSat to provide information on cloud top and base. However,  
190 CloudSat is not as sensitive to clouds as CALIOP. In particular, CloudSat is affected by  
191 ground clutter in the lower 800 m of the atmosphere (Marchand et al. 2008), which limits  
192 its ability to detect low-level liquid cloud. In order to reduce the amount of profiles with  
193 large errors in the inputs to our radiative transfer calculations, we discard from our analysis  
194 CERES FOVs when the following three conditions are met: CALIOP is not operational, the  
195 reported CERES footprint cloud fraction is smaller than 0.25, and the difference between  
196 the measured and estimated fluxes for the CERES footprint is larger than  $100 \text{ W m}^{-2}$ . The  
197  $100 \text{ W m}^{-2}$  threshold is a conservative choice, so the results may still contain a small fraction  
198 of points affected by inputs with large errors. These three conditions have to be met at the  
199 same time for rejection. The non-availability of the CALIPSO lidar flags a higher risk of  
200 scene misidentification. We add two additional constraints to minimise the amount of points  
201 filtered out. Only 2% of the points are discarded. Although this may introduce some small  
202 biases, it is a better approach than keeping points with large scene identification errors that  
203 would introduce large spurious biases in the radiative transfer calculations.

204 *c. Cloud top phase identification*

205 Huang et al. (2012, 2015) examine a variety of cloud phase products at high latitudes.  
206 While they find significant differences between products, they all show a large occurrence  
207 of supercooled liquid water over the southern oceans, with a large fraction of all liquid  
208 topped clouds being supercooled, in line with the results from earlier studies (Hu et al.  
209 2010). In order to understand the sensitivity of our results to the uncertainties in cloud top  
210 phase identification, we compare here results from three different methods. Our standard  
211 algorithm (referred to as Method 1) uses the vertical profiles of temperature (CCCM-77),  
212 LWC (CCCM-85) and IWC (CCCM-86) in the uppermost cloud level of each cloud group.  
213 In order to understand the impact of the cloud top phase identification in the results, we  
214 also use two additional algorithms. The second method (Method 2) looks at each cloud  
215 group in a CERES footprint and uses the uppermost cloud top water phase derived from  
216 MODIS (Minnis et al. 2011, CCCM-34). Because CALIPSO/CloudSat and MODIS are  
217 not necessarily seeing the same cloud, we only include points when cloud top heights from  
218 CALIPSO/CloudSat and MODIS are within 1 km for high clouds ( $\text{top} > 6.5 \text{ km}$ ), within 0.5  
219 km for mid-level clouds ( $6.5 \text{ km} \geq \text{top} > 3.5 \text{ km}$ ), and within 0.2 km for low clouds ( $\text{top} \leq$   
220  $3.5 \text{ km}$ ). Method 3 uses a more conventional way of cloud top phase identification. It uses  
221 MODIS only, which identifies one or two cloud layers in a CERES footprint and derives the  
222 water phase. Since several cloud layers can co-exist within 20 km of a CERES footprint, more  
223 than one cloud top heights can be reported from MODIS. SSF and CCCM products include  
224 up to two non-overlapping cloud top heights in a CERES footprint (Minnis et al. 2011).  
225 Both cloud top phase (SSF-107) and cloud top temperature (CTT; SSF-97) from MODIS  
226 are used. Any cloud that is classified as liquid and whose cloud top temperature is below  $0^\circ\text{C}$   
227 is then classified as supercooled. Method 1 and 2 obtain the cloud top temperature from the  
228 reanalysis temperature (CCCM-77) at cloud top height. Method 3 uses the MODIS-derived  
229 cloud top temperature (SSF-97). Table 2 summarises the three methods.

230 The three methods give large differences in the probability of cloud top phase identifica-

tion (Figure 2). However, the three methods are consistent with recent studies that show a large occurrence of supercooled liquid water over the southern oceans, with a large fraction of all liquid topped clouds being supercooled (Hu et al. 2010; Huang et al. 2015). The fractions of clouds (with respect to the total cloud fraction) with liquid tops between  $-40^{\circ}\text{C}$  and  $0^{\circ}\text{C}$  are 0.8, 0.84, and 0.60, respectively for the three methods. Total cloud fraction derived from MODIS is generally smaller than that derived from CALIPSO/CloudSat. Once thin clouds that are below detection limit of MODIS are excluded, cloud fractions agree to within 0.1 (Figure 11 of Kato et al. (2011)). If only MODIS is used (Method 3), it is difficult to screen thin ice clouds that might influence phase identification on lower-water clouds. This might be one of the reasons why Method 3 shows smaller frequency of occurrence of supercooled water. If we restrict the lower temperature to  $-20^{\circ}\text{C}$ , these fractions are 0.88, 0.86, and 0.67. Hu et al. (2010) estimate that, over the Southern Oceans, more than 85% of the clouds contain liquid phase for temperatures above  $-20^{\circ}\text{C}$ . Our cloud top phase classification method gives a comparable result for the average fraction of clouds with supercooled liquid tops. Figure 2 illustrates the current limits of remote observations of cloud-top thermodynamic phase. For instance, Method 1 shows a much smaller fraction for temperatures below  $-20^{\circ}\text{C}$  compared to the other two methods, potentially due to the use of CCCM liquid and ice water contents. Cloud retrievals based on passive imagers can also be affected by large biases, especially at large solar zenith angles (e.g. Grosvenor and Wood 2014). However, despite these uncertainties, the fact that all methods report large fractions of supercooled liquid for temperatures above  $-20^{\circ}\text{C}$  gives robustness to the results presented below.

#### 252 *d. Model simulations*

253 We use model simulations from the CMIP5 (Taylor et al. 2012). We analyse outputs from  
254 atmosphere-only experiments from 23 models: bcc-csm1-1, bcc-csm1-1-m, CCSM4, CESM1-  
255 CAM5, CNRM-CM5, CSIRO-Mk3-6-0, CanAM4, FGOALS-s2, GFDL-HIRAM-C180, GFDL-  
256 HIRAM-C360, GISS-E2-R, HadGEM2-A, inmcm4, IPSL-CM5A-LR, IPSL-CM5A-MR, IPSL-

257 CM5B-LR, MIROC5, MPI-ESM-LR, MPI-ESM-MR, MRI-AGCM3-2H, MRI-AGCM3-2S,  
258 MRI-CGCM3, and NorESM1-M. The atmosphere-only experiments are run following the At-  
259 mospheric Model Intercomparison Project protocol (AMIP; Gates 1992). They use present-  
260 day boundary conditions and forcings: sea-surface temperatures (SSTs), sea-ice, and green-  
261 house gases.

262 We also perform 2.2km-resolution simulations of a Southern Ocean cyclone with a local-  
263 area configuration of the Met Office Unified Model. Two simulations were performed with  
264 heterogeneous ice nucleation occurring below  $T_{nuc} = 0^{\circ}C$  and  $T_{nuc} = -40^{\circ}C$ , respectively.  
265 The simulations are performed over a 30x30 degree area centred on (52°S, 0°E) on 9th Decem-  
266 ber 2014. The model fields were analysed at 1-hour intervals between 11UTC and 13UTC,  
267 for a forecast initialised at 0UTC. Since we carry out a sensitivity experiment changing the  
268 heterogeneous freezing temperature, we give a brief description of the model’s microphysical  
269 scheme here. The Unified Model microphysics is a single moment bulk microphysics repre-  
270 sentation. It is based on Wilson and Ballard (1999), with extensive modifications (e.g. Abel  
271 et al. 2010). Liquid and ice mass mixing ratios are prognostics with explicit rate equations  
272 controlling the transfer of water between ice, liquid and vapour phases. Loss of supercooled  
273 liquid can occur through evaporation, riming and nucleation. Homogeneous freezing occurs  
274 at temperatures colder than  $-40^{\circ}C$  and freezes all of the water in the grid box. Heterogeneous  
275 freezing occurs for temperatures colder than  $-10^{\circ}C$  (in the operational configuration) and  
276 only when liquid water is present. This process seeds an amount of ice mass dependent on  
277 the temperature.

#### 278 *e. Cyclone compositing*

279 We use the cyclone compositing methodology of Field and Wood (2007). Minima in  
280 daily mean sea level pressure are identified over the latitudes 40°S-70°S. A box covering  
281 60 degrees in longitude and 30 degrees in latitude is centred on the cyclone. This box is  
282 large enough that mature cyclones, and to some extent transient ridges ahead or behind

283 the cyclone, can be included, but not so large to be seriously affected by a following large  
284 cyclone. Previous studies have found that two years of data give robust results. More details  
285 on this methodology are given in Field and Wood (2007) and Bodas-Salcedo et al. (2012).

### 286 **3. Results**

287 We use data from passive and active instruments from the A-Train (Stephens et al. 2002),  
288 and radiative transfer simulations to quantify the contribution of different cloud types to  
289 the radiation budget over the entire Southern Ocean. We process data for five Southern  
290 Hemisphere summers (December, January, February), from December 2006 to February  
291 2011 (except January 2011 due to missing data). We classify each profile (or 'cloud group')  
292 according to how the clouds are distributed in the vertical, following the Cloud Vertical  
293 Structure (CVS) proposed by Tselioudis et al. (2013). The atmospheric column is divided  
294 into 3 layers, with pressure boundaries at 440 hPa and 680 hPa. This follows the widely  
295 used division proposed by the International Satellite Cloud Climatology Project (Rossow  
296 and Schiffer 1999). The layers are labelled as follows: H for the high layer, M for the middle  
297 layer, and L for the lower layer. A CVS is then a combination of the layers that contain cloud.  
298 For instance, the CVS labelled as HM will contain profiles with clouds in the higher and  
299 middle layers. Profiles in which a cloud extends across the pressure boundary between layers  
300 include an 'x' between the layers' names. For instance, MxL contains cloud in the middle  
301 and lower layers, with a cloud layer that extends across the 680 hPa pressure boundary.  
302 We also classify each profile by the cloud top phase of the uppermost cloud layer (Method  
303 1 above). For each CVS, we have four phase categories: liquid (LIQ), supercooled liquid  
304 (SCL), mixed-phase (MIX), and ice (ICE). We also calculate statistics for clear-sky profiles  
305 (CLR). We calculate the area fraction of each combination of CVS and cloud top phase,  
306 shown in the grey stacked histogram in Figure 3a. The sum of all the bars is one. All the  
307 values quoted here are calculated over the population of CERES footprints analysed. The

308 Southern Ocean is covered with cloud around 87% of the time. This value is comparable  
309 to other (spatially-complete) estimates, which reinforces the idea that the CERES FOV  
310 filtering is not introducing a significant selection bias. Profiles with only cloud in the lower  
311 (L) layer are the most frequent CVS, with one third of the population. Low-, mid-, and  
312 high-top cloud account for 33%, 17%, and 37% of the cloud fraction, respectively. We  
313 use the radiative transfer simulations described above to quantify the contribution of each  
314 CVS-phase combination to the TOA shortwave radiation budget (colour stacked histogram in  
315 Figure 3a). The total radiative contribution of a CVS depends on its frequency of occurrence  
316 and on the average reflected flux when present. The sum of all the colour bars gives a cloud-  
317 fraction and area-weighted average flux of  $380 \text{ W m}^{-2}$ . This is not an estimate of the true  
318 climatological December-January-February (DJF) average because the temporal sampling is  
319 not homogeneous through the diurnal cycle. The main result from these calculations is that  
320 clouds containing supercooled liquid water at their tops contribute 30% of the total reflected  
321 flux, whereas clouds with ice, and liquid, and mixed-phase tops contribute 45%, 11%, and  
322 6%.

323 The distribution of cloud top phase shows a latitudinal dependence (Figure 3b). Super-  
324 cooled liquid clouds show a maximum in occurrence between 60 and 65 degrees South, and  
325 are the most frequent category between 55 and 68 degrees South. South of 60°S virtually  
326 all liquid clouds are supercooled, and supercooled clouds dominate the population of liquid  
327 clouds poleward of 48°S. Ice clouds dominate the contribution to the TOA flux at all lati-  
328 tudes, except between 60°S and 65°S, where supercooled liquid clouds lead the contribution  
329 to the TOA reflected flux.

330 It is worth mentioning that the identification of cloud top and base in CCCM is primarily  
331 based on CALIOP derived cloud profiles (Kato et al. 2010), which minimises the impact of  
332 ground clutter in the CloudSat signal. When cloud base is not available from CloudSat  
333 and CALIOP is completely attenuated the CALIOP lowest unattenuated base is chosen.  
334 The optical thickness for cloud groups is scaled to match the optical thickness derived from

335 MODIS. This means that there will be more uncertainties in multi-layer situations where  
336 the CALIOP signal is attenuated before reaching the lower layers. In this case, the scaling  
337 of MODIS optical thickness will still retain the radiative impact of the total cloud column,  
338 but the cloud layers below the attenuation level will be missed from the vertical distribution  
339 of condensate. We therefore expect some underestimation in the frequency of occurrence of  
340 CVSs with clouds in all three layers, in favour of those with clouds in the H and M layers.  
341 This reinforces the role of clouds with tops in the lower and mid-level layers.

342 In Section 2c, we have estimated the fraction of clouds with supercooled liquid tops from  
343 three different methods. For the range of temperatures between  $-40^{\circ}\text{C}$  and  $0^{\circ}\text{C}$ , this fraction  
344 is between 60% for Method 3 and 84% for Method 2, with the standard method giving a value  
345 of 80%. Figure 3a shows that the contribution of each CVS to the total shortwave reflected  
346 flux (colour bars) is very well correlated with its frequency of occurrence (gray bars). We use  
347 this fact and the supercooled liquid fractions from the three methods to estimate that clouds  
348 with supercooled liquid tops contribute between 23% and 32% of the total reflected flux.  
349 Since the partition between mixed-phase and supercooled liquid is uncertain, it is probably  
350 more robust to add the SLW and MIX categories together. The contribution of both classes  
351 goes from 27% to 38%.

352 The Northern Hemisphere oceans do not show such a large frequency of occurrence  
353 of supercooled liquid cloud (Hu et al. 2010; Huang et al. 2012, 2015), which poses the  
354 question of what controls the differences in the observed distribution of cloud phase in both  
355 hemispheres. The Southern Ocean shows large amounts of cloud liquid water in summer,  
356 with average temperatures ranging between  $-10$  and  $0^{\circ}\text{C}$  (Figure 4). The  $0^{\circ}\text{C}$  isotherm  
357 is located much farther polewards over the Northern Hemisphere in summer due to the  
358 warmer SSTs for the same latitude band. The Southern Ocean summer lower troposphere  
359 stays in a range of temperatures that favours the existence of supercooled liquid clouds.  
360 Huang et al. (2015) suggest that the difference in the occurrence of supercooled liquid cloud  
361 between the southern and northern ocean mid-latitudes in their respective summer seasons



362 is fundamentally controlled by the thermodynamics. We investigate this by comparing the  
363 frequency distributions of liquid cloud top temperatures in the summer season in the mid-  
364 latitude oceans in both hemispheres (Figure 5a). We restrict the analysis to ocean points  
365 between 50°S and 60 degrees latitude, where the occurrence of supercooled liquid is maximum  
366 in the Southern Hemisphere. Consistent with the zonal mean cross section of cloud liquid  
367 water content (Figure 4), the Northern Hemisphere clouds are warmer than those over the  
368 Southern Ocean within the same latitude range. It is also important to notice that the  
369 shapes of the distributions are very different, with the Northern Hemisphere distribution  
370 being negatively skewed. This may be due to gross thermodynamic structural differences  
371 and/or suggest a possible role of aerosol-cloud interactions in controlling the differences in  
372 cloud phase between both hemispheres. It is worth mentioning that the Southern Ocean  
373 seems to show smaller values of LWC than the Northern Hemisphere oceans below 500 m.  
374 It is not obvious why this difference exists, and it might just be an artefact of the CCCM  
375 dataset.

376 We attempt to remove the influence of the gross thermodynamic difference by imposing  
377 the same SST distribution in both hemispheres. We randomly sample cloud top temperatures  
378 such that the populations in both hemispheres have the same underlying SST distribution  
379 (Figure 5b). We impose a constant (top-hat) SST distribution in the SST range where  
380 the two original distributions overlap, between 0°C and 10°C. The large skewness in the  
381 Northern Hemisphere distribution of CTTs disappears, and both hemispheres show a very  
382 similar shape. However, the distribution in the Southern Hemisphere is still shifted to colder  
383 temperatures by 4°C. A two-tailed t-test shows that the means of these two distributions  
384 are not equal at a 0.01 level of significance.

385 Although gross thermodynamic differences (characterised here by the distribution of local  
386 SSTs) explain a large part of the differences between both hemispheres, there are other  
387 processes that may contribute to the inter-hemispheric differences. As mentioned above,  
388 one possible candidate is the role of aerosol-cloud interactions, driven by the large inter-

389 hemispheric differences in the amount and composition of aerosols. The Southern Ocean is  
390 a pristine environment, with small amounts of dust that can act as ice nuclei (Choi et al.  
391 2010). This limitation in ice nuclei over the Southern Ocean may contribute to enhancing the  
392 population of supercooled clouds for the same temperature range. We assess this by studying  
393 the sensitivity to ice nucleation of model clouds in the 2.2km-resolution simulations of a  
394 Southern Ocean cyclone described in Section d (Figure 5c). We choose a case that contains  
395 a midlatitude cyclone in the Southern Ocean, as previous studies have shown that these  
396 systems contain clouds that contribute to the southern ocean shortwave bias (Bodas-Salcedo  
397 et al. 2014). The purpose of this experiment is to demonstrate the effects on liquid and ice  
398 water content of limiting the amount of heterogeneous ice nucleation, and therefore we do  
399 not present here an evaluation of the simulations against observations.

400 The histograms of liquid cloud-top temperature show a bimodal distribution. For  $T_{nuc} =$   
401  $0^{\circ}C$  (solid line), the cold mode peaks around  $-7^{\circ}C$ , indicative of the temperature range of  
402 the boundary layer clouds in the simulations. For  $T_{nuc} = -40^{\circ}C$  (dashed line), the tail  
403 of the histogram is shifted a few degrees towards colder temperatures, showing that colder  
404 liquid cloud-tops are more prevalent if ice nucleation is inhibited. The fraction of grid points  
405 with cloud top below 8.4km that has liquid water cloud top colder than  $-10$  increase from  
406 0.12 for  $T_{nuc} = 0^{\circ}C$  to 0.28 for  $T_{nuc} = -40^{\circ}C$ . The frequency of points with liquid clouds  
407 at  $-10^{\circ}C$  is increased by a factor of 3. Since the total number of points that go into the  
408 calculations of the normalised distributions is only 10% larger for  $T_{nuc} = -40^{\circ}C$ , large  
409 differences in the frequency for a given temperature imply large differences in the number  
410 of liquid clouds. The small increase in the total number of points contributes to explaining  
411 the reduction in frequency of the warm mode. The shift of the supercooled liquid mode is  
412 consistent with the observational results in Figure 5b.  $T_{nuc} = -40^{\circ}C$  may be considered an  
413 extreme perturbation, but for this case study the top of layer clouds with supercooled water  
414 in the cold sector of the cyclone only reach up to  $-10^{\circ}C$  due to the subsidence in this sector  
415 of the cyclone. It is worth noting that in the real world, CALIPSO reports supercooled

416 liquid down to  $-25^{\circ}\text{C}$  near the warm front. Despite that both simulations have trouble  
417 producing super-cooled liquid water as compared to CALIPSO, the effect of limiting the  
418 amount of heterogeneous ice nucleation is consistent with the inter-hemispheric differences  
419 shown in Figure 5b. Setting the freezing temperature to  $-20^{\circ}\text{C}$  or even  $-10^{\circ}\text{C}$  makes only  
420 small differences to the character of the results. The frontal clouds that have cloud tops  
421 extending to much colder levels are not affected and are glaciated down to the melting level.  
422 Therefore the effects of changing the heterogeneous freezing temperature will largely be seen  
423 on the frequency of occurrence of supercooled liquid water at these temperatures rather than  
424 seeing large frequencies of occurrence at much colder temperatures.

425 This modeling evidence suggests that microphysical processes also play a role in the  
426 observed inter-hemispheric differences of supercooled liquid clouds. However, our character-  
427 isation of the thermodynamic state is very basic. For instance, although we have restricted  
428 this analysis to ocean points, the Northern Hemisphere contains large areas of land that  
429 not only impact the aerosol distribution, but also the vertical thermodynamic structure of  
430 air advected over the oceans that cannot be fully captured by the underlying SSTs. There-  
431 fore, more needs to be done to disentangle the thermodynamic, dynamic and microphysical  
432 contributions to the observed inter-hemispheric differences in cloud phase.

433 Since the representation of the physical processes that control cloud phase are poorly  
434 represented in models, the results presented here may have consequences for climate sim-  
435 ulations. It is also worth noting that, even if models are able to reproduce the observed  
436 distribution of cloud condensate, the correct simulation of cloud phase is also important, as  
437 liquid clouds are brighter than ice clouds for a given water path. We analyse results from 23  
438 atmosphere-only climate models (see Section d for details). We compare the DJF reflected  
439 shortwave radiation from the AMIP experiment against observations from the CERES EBAF  
440 climatology (Figure 6). The ensemble shows a strong negative bias between  $60$  and  $70^{\circ}\text{S}$ ,  
441 where the amount of supercooled liquid cloud is maximum in the observations. In this re-  
442 gion, a majority of models (grey shading) show a deficit in reflected shortwave radiation.

443 It is also noticeable that the Southern Ocean is the region where the models show larger  
444 spread. Previous work has shown that clouds in the cold-air side of cyclones are mainly  
445 responsible for these biases (Bodas-Salcedo et al. 2014). Cyclone composite analysis of the  
446 CCCM cloud top phase data shows that this area of the cyclone composite contains large  
447 amounts of supercooled liquid clouds (Figure 7). The poleward side of the cyclones is still  
448 dominated by clouds with ice tops. However, the total condensate in the poleward side is  
449 not dominated by ice, with the average liquid water path being similar or larger than the  
450 ice water path (Figures 8a and 9a). This suggests that the liquid phase probably dominates  
451 the contribution to the TOA shortwave flux in this region of the cyclones.

452 Figures 8 and 9 also show model composites of cloud liquid and ice water paths. Only  
453 a subset of the 23 models included in Figure 6 submitted the necessary daily diagnostics  
454 to do the cyclone composite analysis. Models tend to show a very poor representation  
455 of cloud liquid water path (LWP) (Figure 8). Half of the models tend to underestimate  
456 cloud LWP in the cold-air region of the cyclone composites. The models that show less  
457 LWP in the cold sector (CNRM-CM5, HadGEM2-A, MIROC5, and MRI-CGCM3) also  
458 show the largest shortwave biases (Figure 4 in Bodas-Salcedo et al. (2014)). All the models  
459 overestimate cloud LWP in the warm frontal region of the composite, but this has to be  
460 interpreted with caution. The observations probably underestimate the amount of cloud  
461 liquid water in the warm sector, as this is an area that also contains large quantities of  
462 ice clouds above (Figures 7c and 9a) that will reduce the capability to retrieve cloud liquid  
463 content under thick ice clouds. It is worth mentioning that the cyclone compositing does not  
464 apply a rotation to align the position of the fronts, which makes a very strict definition of  
465 the location of the warm/cold sectors not possible. Figure 3 in Bodas-Salcedo et al. (2014)  
466 shows a schematic of the approximate position of the warm and cold sectors in the cyclone  
467 composite. Roughly speaking, the warm sector occupies the first quadrant (in the standard  
468 trigonometrical definition), but it also extends to parts of the other quadrants.

469 Figure 9 also shows that the models simulation of cloud ice water path is more in line

470 with the observations. They tend to underestimate the ice water path (IWP) in the warm  
471 sector, although CCCM may be an overestimate in this region. Some models show too much  
472 ice in the cold sector, which may partially compensate for the shortwave biases introduced  
473 by the lack of liquid water path. These results show that models have great difficulties  
474 in simulating the correct distribution of cloud condensate, and that they may produce a  
475 decent climatological TOA shortwave radiation budget due to compensating errors in the  
476 distribution of cloud condensate.

477 Analysis of climate change experiments (not shown) show strong negative shortwave  
478 feedbacks in the latitudes where large present-day biases exist. This suggests that the mid-  
479 latitude shortwave negative cloud radiative feedbacks observed in models may be overesti-  
480 mated due to a poor simulation of supercooled liquid clouds in the present day, with potential  
481 implications for our current estimates of climate sensitivity. A detailed analysis of the cloud  
482 responses in these climate change experiments is under way and will be reported elsewhere.

## 483 **4. Conclusions**

484 We have carried out a comprehensive analysis of the role of clouds in the solar radiation  
485 budget over the Southern Ocean. We have used satellite data from the latest generation of  
486 passive and active instruments, and radiative transfer simulations to quantify the contribu-  
487 tion of different cloud types and cloud thermodynamic phase to the TOA radiation budget.  
488 We focus our analysis on the Austral Summer as the main aim of this study is in the solar  
489 part of the spectrum. The methodology presented here can be easily extended to the entire  
490 globe and to the longwave part of the spectrum.

491 This analysis shows that scenes where the uppermost cloud layer contains supercooled  
492 liquid water contribute between 27% to 38% to the total amount of shortwave reflected  
493 radiation in the 40°S to 70°S region. We have investigated the drivers of the differences in  
494 the frequency of occurrence of supercooled liquid between hemispheres in their respective

495 summers, and our results suggest that differences in the thermodynamics of the environment  
496 explain most of the differences, consistent with the findings of previous studies. Other  
497 processes, like ice nucleation, seem to play a secondary role, at least during the summer  
498 months. These results show that a better simulation of supercooled liquid clouds is crucial  
499 for a better representation of the TOA radiation budget over the Southern Ocean, consistent  
500 with the recent modelling study by Kay et al. (submitted).

501 We have investigated the implications of these findings in the context of present-day  
502 climate simulations. We apply cyclone compositing techniques to CMIP5 model data to un-  
503 derstand the implications of these findings in the context of present-day climate simulations  
504 over the Southern Ocean. The poor simulation of supercooled liquid clouds in climate models  
505 is shown to lead to significant model errors. Models that show large shortwave errors in the  
506 cold-air region of the cyclone composites tend to underestimate cloud LWP in that region  
507 of the cyclone composite, where the observations generally show a large frequency of occur-  
508 rence of clouds with supercooled liquid tops exposed to space. Previous studies have shown  
509 that this area of the cyclones is responsible for the Southern Ocean solar radiation biases  
510 (Bodas-Salcedo et al. 2014). Some models show too much ice in the cold sector, which may  
511 partially compensate for the shortwave biases introduced by the lack of liquid water path.  
512 These results show that models have great difficulties in simulating the correct distribution  
513 of cloud condensate, and that they may produce a decent climatological TOA SW radiation  
514 budget due to compensating errors in the spatial distribution of cloud condensate. In order  
515 to connect more directly these results with parameterisation errors, more work needs to be  
516 done to implement model diagnostics that are directly comparable with the results presented  
517 here.

518 These results may undermine our confidence in the large negative cloud feedbacks found  
519 in climate change simulations over the Southern Ocean. Future work should focus on the po-  
520 tential implication of these findings in these large negative feedbacks. It is also important to  
521 coordinate efforts (field campaigns, analysis of remote sensing data, and detailed modelling)

522 if we want to advance our knowledge of the physical processes that control the formation  
523 and evolution of supercooled liquid clouds over the Southern Ocean and to increase our  
524 confidence in simulated cloud feedbacks.

525 *Acknowledgments.*

526 This work was supported by the Joint DECC/Defra Met Office Hadley Centre Climate  
527 Programme (GA01101). We acknowledge the World Climate Research Programme's Work-  
528 ing Group on Coupled Modelling, which is responsible for CMIP, and we thank the cli-  
529 mate modelling groups for producing and making available their model output. For CMIP  
530 the U.S. Department of Energy's Program for Climate Model Diagnosis and Intercom-  
531 parison provides coordinating support and led development of software infrastructure in  
532 partnership with the Global Organization for Earth System Science Portals. CCCM data  
533 were obtained from the NASA Langley Research Center Atmospheric Sciences Data Center  
534 (<http://eosweb.larc.nasa.gov>). We thank M. A. Ringer, T. Andrews, A. Karmalkar, and M.  
535 Webb for their comments.

## REFERENCES

- 538 Abel, S. J., D. N. Walters, and G. Allen, 2010: Evaluation of stratocumulus cloud prediction  
539 in the Met Office forecast model during VOCALS-REx. *Atmos. Chem. Phys.*, **10**, 10541–  
540 10559, doi:10.5194/acp-10-10541-2010.
- 541 Baran, A. J., P. Field, K. Furtado, J. Manners, and A. Smith, 2013: A new high- and  
542 low-frequency scattering parameterization for cirrus and its impact on a high-resolution  
543 numerical weather prediction model. *AIP Conf. Proc.*, 716–719.
- 544 Bennartz, R., et al., 2013: July 2012 Greenland melt extent enhanced by low-level liquid  
545 clouds. *Nature*, **496**, 83–86, doi:10.1038/nature12002.
- 546 Bloom, S. C., A. da Silva, and D. Dee, 2005: Documentation and validation of the Goddard  
547 Earth Observing System (GEOS) Data Assimilation System version 4. Tech. Rep. , NASA  
548 Goddard Space Flight Center. NASA Technical Memorandum 104606.
- 549 Bodas-Salcedo, A., K. D. Williams, P. R. Field, and A. P. Lock, 2012: The surface down-  
550 welling solar radiation surplus over the Southern Ocean in the Met Office model: the role  
551 of midlatitude cyclone clouds. *J. Climate*, **25**, 7467–7486, doi:10.1175/JCLI-D-11-00702.1.
- 552 Bodas-Salcedo, A., et al., 2014: Origins of the solar radiation biases over the Southern Ocean  
553 in CFMIP2 models. *J. Climate*, **27**, 41–56, doi:10.1175/JCLI-D-13-00169.1.
- 554 Ceppi, P., Y.-T. Hwang, D. M. W. Frierson, and D. L. Hartmann, 2012: Southern Hemi-  
555 sphere jet latitude biases in CMIP5 models linked to shortwave cloud forcing. *Geophys.*  
556 *Res. Lett.*, **39**, L19708, doi:10.1029/2012GL053115.



557 Cesana, G., J. E. Kay, H. Chepfer, J. M. English, and G. de Boer, 2012: Ubiquitous low-  
558 level liquid-containing Arctic clouds: New observations and climate model constraints  
559 from CALIPSO-GOCCP. *Geophys. Res. Lett.*, **39**, L20 804, doi:10.1029/2012GL053385.

560 Choi, Y.-S., R. S. Lindzen, C.-H. Ho, and J. Kim, 2010: Space observations of cold-  
561 cloud phase change. *Proc. Natl. Acad. Sci. USA*, **107**, 11 211–11 216, doi:10.1073/pnas.  
562 1006241107.

563 Edwards, J. M. and A. Slingo, 1996: Studies with a flexible new radiation code. I: Choosing  
564 a configuration for a large-scale model. *Q. J. R. Meteorol. Soc.*, **122**, 689–720.

565 Field, P. R. and R. Wood, 2007: Precipitation and cloud structure in midlatitude cyclones.  
566 *J. Climate*, **20** (2), 233–254, doi:10.1175/JCLI3998.1.

567 Forbes, R. M. and M. Ahlgrim, 2014: On the representation of high-latitude boundary layer  
568 mixed-phase cloud in the ECMWF global model. *Mon. Weather Rev.*, **142**, 3425–3445,  
569 doi:10.1175/MWR-D-13-00325.1.

570 Gates, W., 1992: The atmospheric model intercomparison project. *Bull. Am. Meteorol. Soc.*,  
571 **73**, 1962–1970.

572 Gregory, D. and D. Morris, 1996: The sensitivity of climate simulations to the specification  
573 of mixed phase clouds. *Clim. Dyn.*, **12**, 641–651.

574 Grosvenor, D. P. and R. Wood, 2014: The effect of solar zenith angle on MODIS cloud optical  
575 and microphysical retrievals within marine liquid water clouds. *Atmos. Chem. Phys.*, **14**,  
576 7291–7321, doi:10.5194/acp-14-7291-2014.

577 Haynes, J. M., T. H. V. Haar, T. L’Ecuyer, and D. Henderson, 2013: Radiative heating char-  
578 acteristics of Earth’s cloudy atmosphere from vertically resolved active sensors. *Geophys.*  
579 *Res. Lett.*, **40** (), 624–630, doi:10.1002/grl.50145.

580 Hogan, R. J., P. N. Francis, H. Flentje, A. J. Illingworth, M. Quante, and J. Pelon, 2003:  
581 Characteristics of mixed-phase clouds. I: Lidar, radar and aircraft observations from  
582 CLARE'98. *Q. J. R. Meteorol. Soc.*, **129**, 2089–2116, doi:10.1256/qj.01.208.

583 Hu, Y., S. Rodier, K. man Xu, W. Sun, J. Huang, B. Lin, P. Zhai, and D. Josset,  
584 2010: Occurrence, liquid water content, and fraction of supercooled water clouds from  
585 combined CALIOP/IIR/MODIS measurements. *J. Geophys. Res.*, **115**, D00H34, doi:  
586 10.1029/2009JD012384.

587 Huang, Y., A. Protat, S. T. Siems, and M. J. Manton, 2015: A-Train observations of maritime  
588 mid-latitude storm-track cloud systems: comparing the Southern Ocean against the North  
589 Atlantic. *J. Climate*, **28** (), 1920–1939, doi:10.1175/JCLI-D-14-00169.1.

590 Huang, Y., S. T. Siems, M. J. Manton, A. Protat, and J. Delano'e, 2012: A study on the low-  
591 altitude clouds over the Southern Ocean using the DARDAR-MASK. *J. Geophys. Res.*,  
592 **117**, D18 204, doi:10.1029/2012JD017800.

593 Hwang, Y.-T. and D. M. W. Frierson, 2013: Link between the double-Intertropical Con-  
594 vergence Zone problem and cloud biases over the Southern Ocean. *Proc. Natl. Acad. Sci.*  
595 *USA*, **110**, 4935–4940, doi:10.1073/pnas.1213302110.

596 Kato, S., S. Sun-Mack, W. F. Miller, F. G. Rose, Y. Chen, P. Minnis, and B. A. Wielicki,  
597 2010: Relationships among cloud occurrence frequency, overlap, and effective thickness  
598 derived from CALIPSO and CloudSat merged cloud vertical profiles. *J. Geophys. Res.*,  
599 **115**, D00H28, doi:10.1029/2009JD012277.

600 Kato, S., et al., 2011: Improvements of top-of-atmosphere and surface irradiance computa-  
601 tions with calipso-, cloudsat-, and modis-derived cloud and aerosol properties. *J. Geophys.*  
602 *Res.*, **116** (D19), D19 209, doi:10.1029/2011JD016050.

603 Kay, J. E., V. Yettella, B. Medeiros, C. Hannay, and P. Caldwell, submitted: Global climate

604 impacts of fixing the Southern Ocean shortwave radiation bias in the Community Earth  
605 System Model (CESM). *J. Climate*, ().

606 Kristjansson, J. E., J. M. Edwards, and D. L. Mitchell, 1999: A new parameterization  
607 scheme for the optical properties of ice crystals for use in general circulation models of the  
608 atmosphere. *Phys. Chem. Earth*, **24**, 231–236, doi:10.1016/S1464-1909(98)00043-4.

609 L’Ecuyer, T. S., N. B. Wood, T. Haladay, G. L. Stephens, and P. W. Stackhouse, 2008:  
610 Impact of clouds on atmospheric heating based on the R04 CloudSat fluxes and heating  
611 rates data set. *J. Geophys. Res.*, **113** (D8), D00A15, doi:10.1029/2008JD009951.

612 Loeb, N. G., S. Kato, K. Loukachine, and N. Manalo-Smith, 2005: Angular distribution  
613 models for top-of-atmosphere radiative flux estimation from the Clouds and the Earths  
614 Radiant Energy System instrument on the Terra satellite. part I: methodology. *J. Atmos.*  
615 *Oceanic Technol.*, **22**, 338–351, doi:10.1175/JTECH1712.1.

616 Loeb, N. G., B. A. Wielicki, D. R. Doelling, S. Kato, T. Wong, G. L. Smith, D. F. Keyes,  
617 and N. Manalo-Smith, 2009: Toward optimal closure of the Earth’s top-of-atmosphere  
618 radiation budget. *J. Climate*, **22** (3), 748–766, doi:10.1175/2008JCLI2637.1.

619 Marchand, R., G. G. Mace, T. Ackerman, and G. L. Stephens, 2008: Hydrometeor detection  
620 using Cloudsat - an Earth-Orbiting 94-GHz cloud radar. *J. Atmos. Oceanic Technol.*, **25**,  
621 519–533, doi:10.1175/2007JTECHA1006.1.

622 Minnis, P., et al., 2011: CERES Edition-2 cloud property retrievals using TRMM VIRS and  
623 Terra and Aqua MODIS data - Part I: Algorithms. *IEEE Trans. Geosci. Remote Sensing*,  
624 **49** (11), 4374–4400, doi:10.1109/TGRS.2011.2144601.

625 Rienecker, M. M., et al., 2008: The GEOS-5 Data Assimilation System - Documentation of  
626 versions 5.0.1 and 5.1.0, and 5.2.0. Tech. Rep. , NASA. NASA/TM-2008-104606.

- 627 Rossow, W. B. and R. A. Schiffer, 1999: Advances in understanding clouds from ISCCP.  
628 *Bull. Am. Meteorol. Soc.*, **80**, 2261–2287.
- 629 Senior, C. A. and J. F. B. Mitchell, 1993: Carbon dioxide and climate: The impact of cloud  
630 parameterization. *J. Climate*, **6**, 393–418.
- 631 Stephens, G. L., et al., 2002: The CloudSat mission and the A-Train. *Bull. Am. Meteorol.*  
632 *Soc.*, **83**, 1771–1790.
- 633 Taylor, K. E., R. J. Stouffer, and G. A. Meehl, 2012: An overview of CMIP5 and the exper-  
634 iment design. *Bull. Am. Meteorol. Soc.*, **93**, 485–498, doi:10.1175/BAMS-D-11-00094.1.
- 635 Tselioudis, G., W. Rossow, Y. Zhang, and D. Konsta, 2013: Global weather states and their  
636 properties from passive and active satellite cloud retrievals. *J. Climate*, **26**, 7734–7746,  
637 doi:10.1175/JCLI-D-13-00024.1.
- 638 Tsushima, Y., et al., 2006: Importance of the mixed-phase cloud distribution in the control  
639 climate for assessing the response of clouds to carbon dioxide increase: a multi-model  
640 study. *Clim. Dyn.*, doi:10.1007/s00382-006-0127-7.
- 641 Williams, K. D. and M. J. Webb, 2009: A quantitative performance assessment of cloud  
642 regimes in climate models. *Clim. Dyn.*, **33** (1), 141–157, doi:10.1007/s00382-008-0443-1.
- 643 Williams, K. D., et al., 2013: The Transpose-AMIP II experiment and its application to  
644 the understanding of Southern Ocean cloud biases in climate models. *J. Climate*, **26**,  
645 3258–3274, doi:10.1175/JCLI-D-12-00429.1.
- 646 Wilson, D. R. and S. P. Ballard, 1999: A microphysically based precipitation scheme for  
647 the UK Meteorological Office Unified Model. *Q. J. R. Meteorol. Soc.*, **125**, 1607–1636,  
648 doi:10.1002/qj.49712555707.
- 649 Winker, D. M., M. A. Vaughan, A. Omar, Y. Hu, K. A. Powell, Z. Liu, W. H. Hunt, and S. A.

650 Young, 2009: Overview of the CALIPSO mission and CALIOP data processing algorithms.  
651 *J. Atmos. Oceanic Technol.*, **26** (11), 2310–2323, doi:10.1175/2009JTECHA1281.1.

## 652 **List of Tables**

- 653     1     Variables from CCCM files used for the radiative transfer calculations. CCCM  
654           files also include variables from the Single Satellite Footprint (SSF) CERES  
655           files. The left column gives the SSF or CCCM index that uniquely identify  
656           the variable. The right column shows the variable names as they appear in  
657           the CCCM files. The names are not fully descriptive. For instance, MODIS  
658           cloud phase is derived from the 3.7, 11 and 12 micron channels, as detailed in  
659           Minnis et al. (2011), not from a single channel. 28
- 660     2     Summary of the three cloud-top phase identification methods. Cloud top  
661           temperature (CTT) is used to distinguish between liquid and supercooled  
662           clouds. 29

TABLE 1. Variables from CCCM files used for the radiative transfer calculations. CCCM files also include variables from the Single Satellite Footprint (SSF) CERES files. The left column gives the SSF or CCCM index that uniquely identify the variable. The right column shows the variable names as they appear in the CCCM files. The names are not fully descriptive. For instance, MODIS cloud phase is derived from the 3.7, 11 and 12 micron channels, as detailed in Minnis et al. (2011), not from a single channel.

Variable	Name
SSF-25	Surface type index
SSF-38	CERES SW TOA flux - upwards
SSF-50	CERES broadband surface albedo
SSF-59	Surface skin temperature
SSF-97	Mean cloud effective temperature for cloud layer
SSF-107	Mean cloud particle phase for cloud layer (3.7)
CCCM-11	Total number of good CALIPSO profiles
CCCM-12	Cloud group area percent coverage
CCCM-13	Cloud layer top level height
CCCM-15	Cloud layer base level height
CCCM-34	Mean group cloud particle phase from MODIS radiance (3.7)
CCCM-76	Pressure profile
CCCM-77	Temperature profile
CCCM-78	Water vapor mixing ratio profile
CCCM-79	Ozone mixing ratio profile
CCCM-84	Cloud extinction coefficient profile used
CCCM-85	Liquid water content profile used
CCCM-86	Ice water content profile used

TABLE 2. Summary of the three cloud-top phase identification methods. Cloud top temperature (CTT) is used to distinguish between liquid and supercooled clouds.

	Method 1	Method 2	Method 3
Liquid	$LWC > 0 \ \& \ IWC = 0$	$CCCM-34 = 1$	$SSF-107 = 1$
Ice	$LWC = 0 \ \& \ IWC > 0$	$CCCM-34 = 2$	$SSF-107 = 2$
Mixed	$LWC > 0 \ \& \ IWC > 0$	$1 < CCCM-34 < 2$	$1 < SSF-107 < 2$
CTT variable	CCCM-77	CCCM-77	SSF-97



## 663 List of Figures

- 664 1 Observed and simulated solar radiative fluxes over the Southern Ocean. (a)  
665 Frequency histograms of the instantaneous reflected solar radiation from the  
666 CCCM data (black), and the radiative transfer calculations (grey). (b) Den-  
667 sity scatter plot of simulations (y axis) versus observations (x axis). (c-d)  
668 are similar to (a-b), but the radiative transfer calculations use the ice optical  
669 properties parameterisation by (Baran et al. 2013). Data from five December-  
670 January-February (2006/12 to 2011/02) seasons over the region 40°S to 72°S  
671 . The observations are instantaneous, footprint measurements of the CERES  
672 instrument at the top of the Atmosphere. The simulations are run on all the  
673 cloud groups observed by the active instruments within each CERES foot-  
674 print, and then weighted by the area fraction. 33
- 675 2 Probability of liquid cloud tops relative to all clouds as function of latitude  
676 and cloud top temperature for three different methods of cloud top phase  
677 identification. Results are for the Southern Hemisphere. 34
- 678 3 Contribution of each cloud type and cloud thermodynamic phase to the solar  
679 radiation budget over the Southern Ocean. a) Vertical profiles are classified  
680 according to their cloud vertical structure (CVS) and cloud top phase. Clear  
681 profiles are labelled as 'CLR'. There are four cloud top phase classes: LIQ  
682 (warm liquid), SCL (supercooled liquid), MIX (mixed-phase), and ICE (ice).  
683 The grey bars show the average frequency of occurrence (left y axis) for each  
684 CVS, partitioned by cloud top phase. The coloured bars show area-fraction-  
685 weighted average of each CVS/phase combination, which represents the con-  
686 tribution of each CVS/phase to the total reflected flux. b) Zonal-mean area  
687 fraction by cloud top phase. The area fraction of clear profiles is displayed in  
688 grey. 35

- 689 4 Ocean-only zonal-mean cross-sections of cloud liquid water content and air  
690 temperature. Summer season average in each hemisphere: December, Jan-  
691 uary, February for the Southern Hemisphere, and June, July, August for the  
692 Northern Hemisphere. Liquid water content is shown in colour, and the line  
693 contours show the air temperature in Celsius. 36
- 694 5 Hemispheric difference of cloud top temperature distributions. Normalised  
695 frequency distributions of liquid cloud top temperatures. Only points with  
696 liquid cloud tops in the uppermost layer are included. (a) and (b) Summer  
697 for the mid-latitude oceans. The distributions are calculated by sampling  
698 ocean points between 50 and 60 degrees of latitude. Southern Ocean in De-  
699 cember, January, February, and Northern Hemisphere basins in June, July,  
700 August. a) Distributions from the entire CCCM population. (b) Distributions  
701 obtained by random sampling imposing a uniform SST distribution. (c) Dis-  
702 tributions from the 2.2-km resolution model simulations with heterogeneous  
703 ice nucleation threshold temperatures of 0°C (solid) and -40°C (dashed). In  
704 (c), liquid cloud-top is defined to be the maximum height at which the liquid  
705 water content is greater or equal than  $10^{-5}kg/kg$ . 37
- 706 6 TOA SW reflected flux error from the CMIP5 AMIP with respect to CERES  
707 EBAF. Zonal-mean averages for Austral Summer (DJF). The solid line shows  
708 the ensemble-mean bias, and the grey envelope the 10th to 90th percentile  
709 range. 38
- 710 7 Cloud top phase frequency of occurrence in Southern Ocean cyclones. Fre-  
711 quency of occurrence composites of cloud top phase around cyclone centres for  
712 December-January-February over the Southern Ocean. CCCM observations  
713 are composited around cyclone centres in a 60° longitude by 30° latitude box  
714 using the method of Field and Wood (2007). The contour lines show compos-  
715 ites of mean sea level pressure (hPa). 39

716	8	Liquid water path around cyclone centres over the Southern Ocean in Austral	
717		Summer (December-January-February). Cyclone composites calculated using	
718		the method of Field and Wood (2007). (a) CCCM data, and (b-j) CMIP5	
719		amip experiment.	40
720	9	Ice water path around cyclone centres over the Southern Ocean in Austral	
721		Summer (December-January-February). Cyclone composites calculated using	
722		the method of Field and Wood (2007). (a) CCCM data, and (b-j) CMIP5	
723		amip experiment.	41

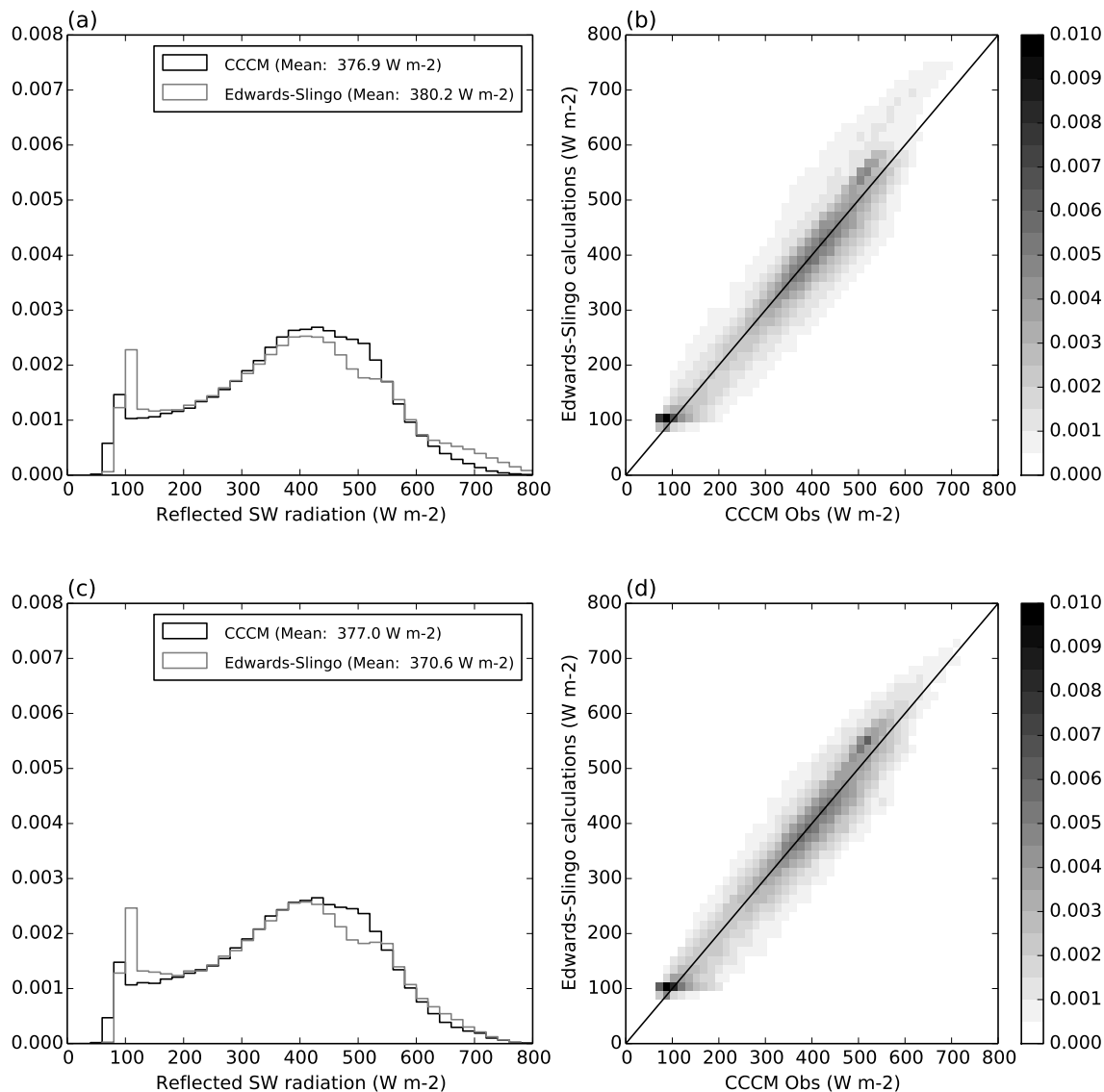


FIG. 1. Observed and simulated solar radiative fluxes over the Southern Ocean. (a) Frequency histograms of the instantaneous reflected solar radiation from the CCCM data (black), and the radiative transfer calculations (grey). (b) Density scatter plot of simulations (y axis) versus observations (x axis). (c-d) are similar to (a-b), but the radiative transfer calculations use the ice optical properties parameterisation by (Baran et al. 2013). Data from five December-January-February (2006/12 to 2011/02) seasons over the region 40°S to 72°S. The observations are instantaneous, footprint measurements of the CERES instrument at the top of the Atmosphere. The simulations are run on all the cloud groups observed by the active instruments within each CERES footprint, and then weighted by the area fraction.

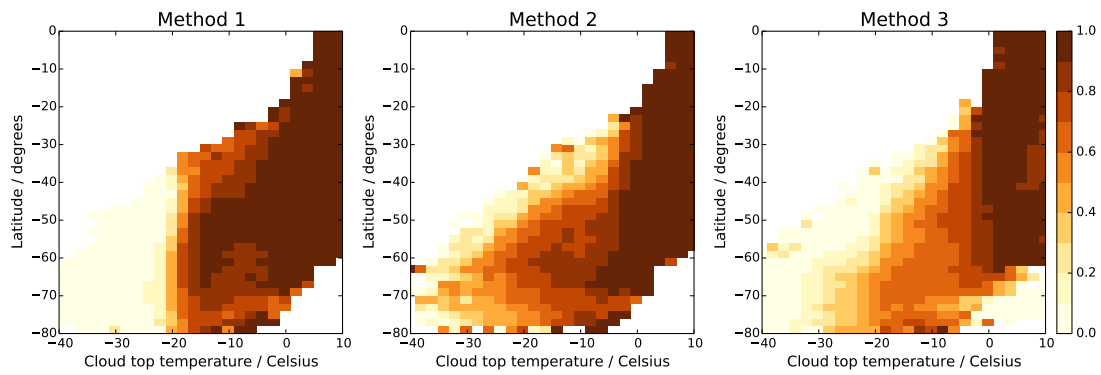


FIG. 2. Probability of liquid cloud tops relative to all clouds as function of latitude and cloud top temperature for three different methods of cloud top phase identification. Results are for the Southern Hemisphere.

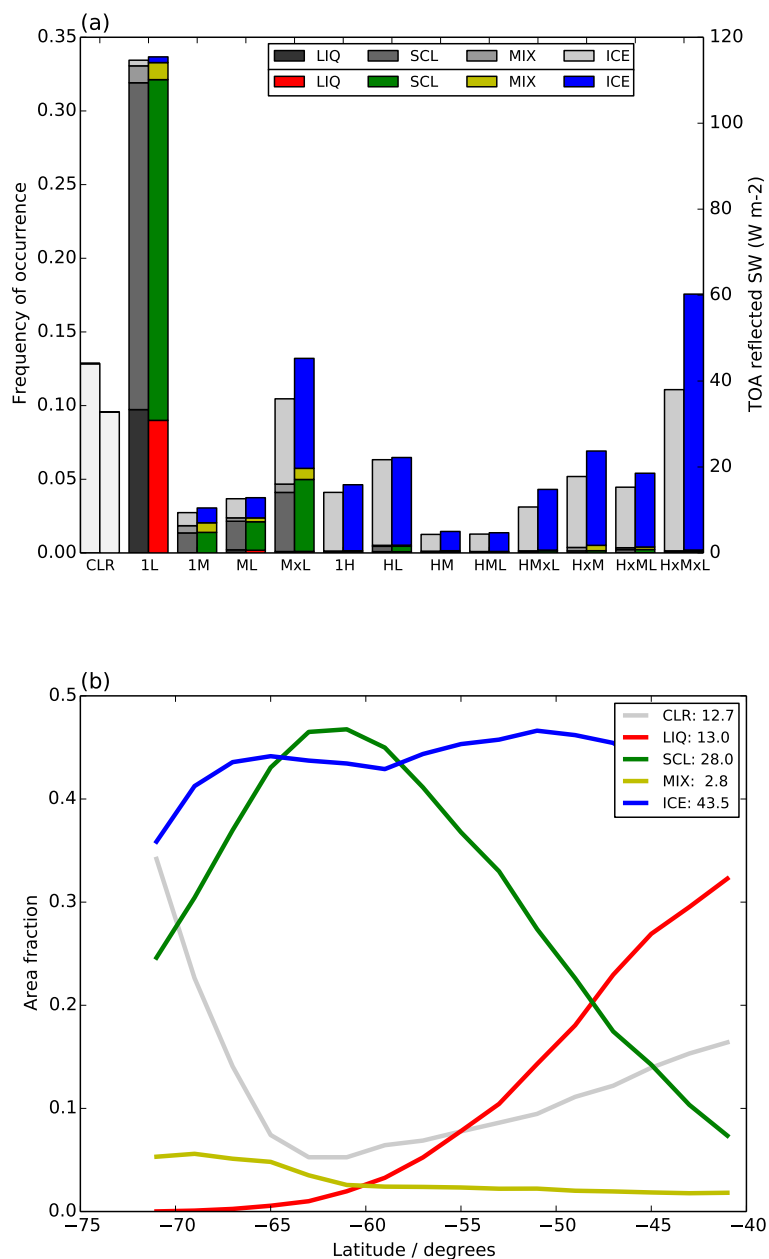


FIG. 3. Contribution of each cloud type and cloud thermodynamic phase to the solar radiation budget over the Southern Ocean. a) Vertical profiles are classified according to their cloud vertical structure (CVS) and cloud top phase. Clear profiles are labelled as 'CLR'. There are four cloud top phase classes: LIQ (warm liquid), SCL (supercooled liquid), MIX (mixed-phase), and ICE (ice). The grey bars show the average frequency of occurrence (left y axis) for each CVS, partitioned by cloud top phase. The coloured bars show area-fraction-weighted average of each CVS/phase combination, which represents the contribution of each CVS/phase to the total reflected flux. b) Zonal-mean area fraction by cloud top phase. The area fraction of clear profiles is displayed in grey.

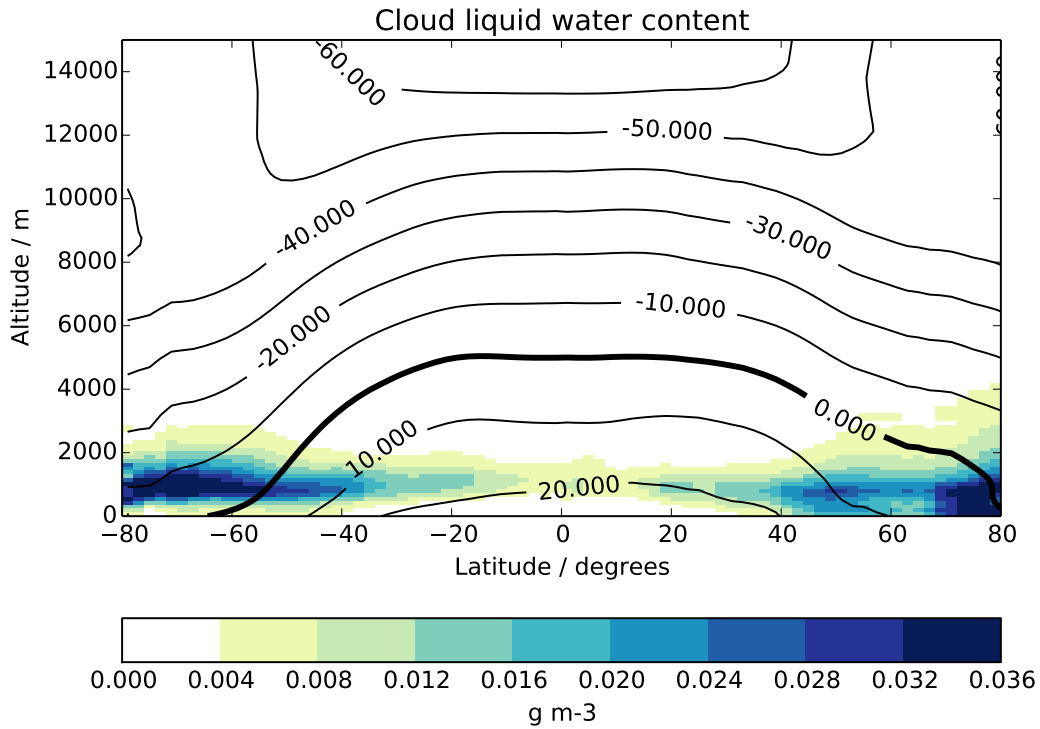


FIG. 4. Ocean-only zonal-mean cross-sections of cloud liquid water content and air temperature. Summer season average in each hemisphere: December, January, February for the Southern Hemisphere, and June, July, August for the Northern Hemisphere. Liquid water content is shown in colour, and the line contours show the air temperature in Celsius.

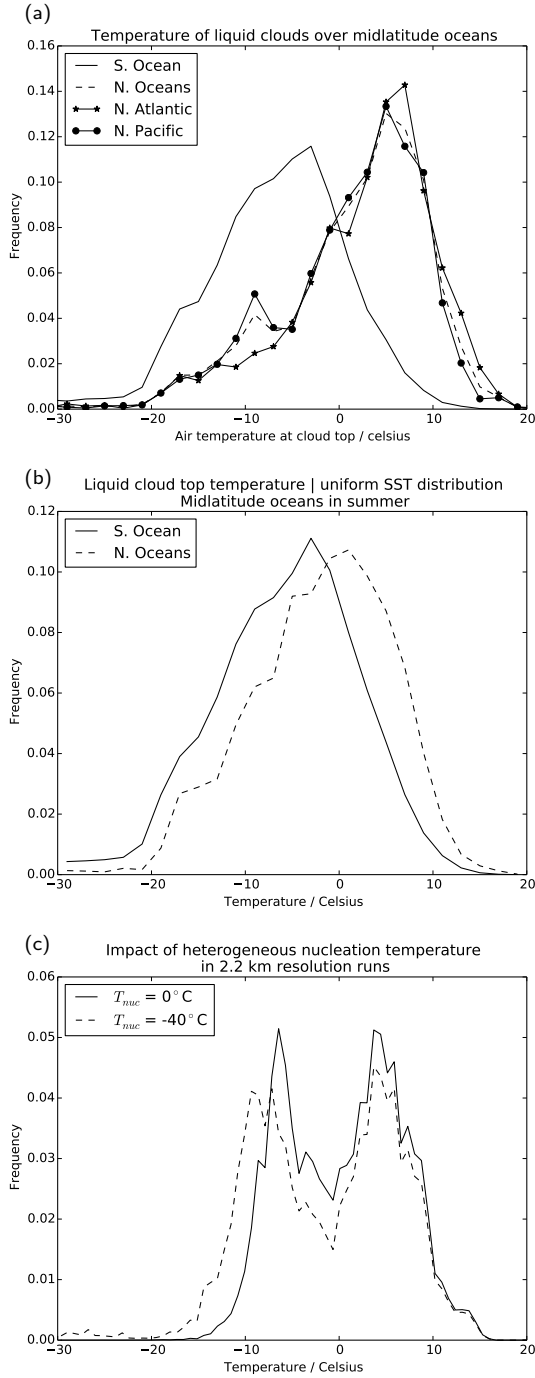


FIG. 5. Hemispheric difference of cloud top temperature distributions. Normalised frequency distributions of liquid cloud top temperatures. Only points with liquid cloud tops in the uppermost layer are included. (a) and (b) Summer for the mid-latitude oceans. The distributions are calculated by sampling ocean points between 50 and 60 degrees of latitude. Southern Ocean in December, January, February, and Northern Hemisphere basins in June, July, August. a) Distributions from the entire CCCM population. (b) Distributions obtained by random sampling imposing a uniform SST distribution. (c) Distributions from the 2.2-km resolution model simulations with heterogeneous ice nucleation threshold temperatures of  $0^\circ\text{C}$  (solid) and  $-40^\circ\text{C}$  (dashed). In (c), liquid cloud-top is defined to be the maximum height at which the liquid water content is greater or equal than  $10^{-5}\text{kg/kg}$ .



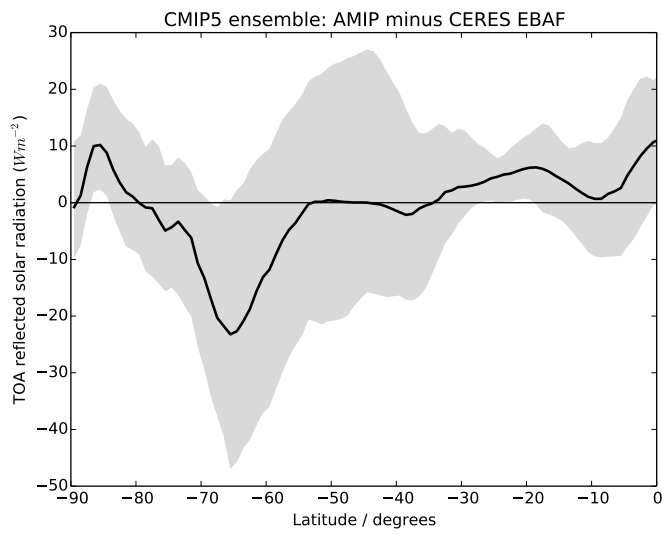


FIG. 6. TOA SW reflected flux error from the CMIP5 AMIP with respect to CERES EBAF. Zonal-mean averages for Austral Summer (DJF). The solid line shows the ensemble-mean bias, and the grey envelope the 10th to 90th percentile range.

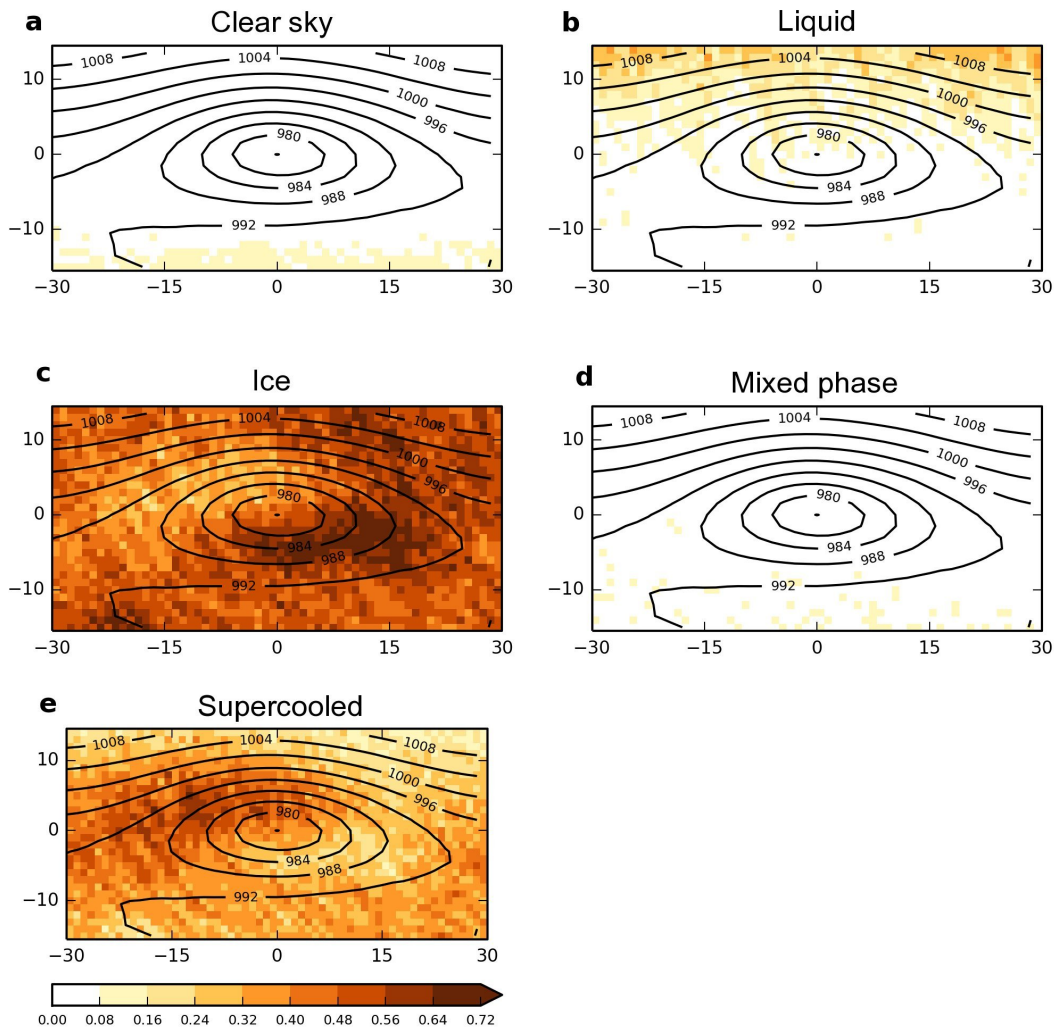


FIG. 7. Cloud top phase frequency of occurrence in Southern Ocean cyclones. Frequency of occurrence composites of cloud top phase around cyclone centres for December-January-February over the Southern Ocean. CCCM observations are composited around cyclone centres in a  $60^\circ$  longitude by  $30^\circ$  latitude box using the method of Field and Wood (2007). The contour lines show composites of mean sea level pressure (hPa).

## Liquid Water Path

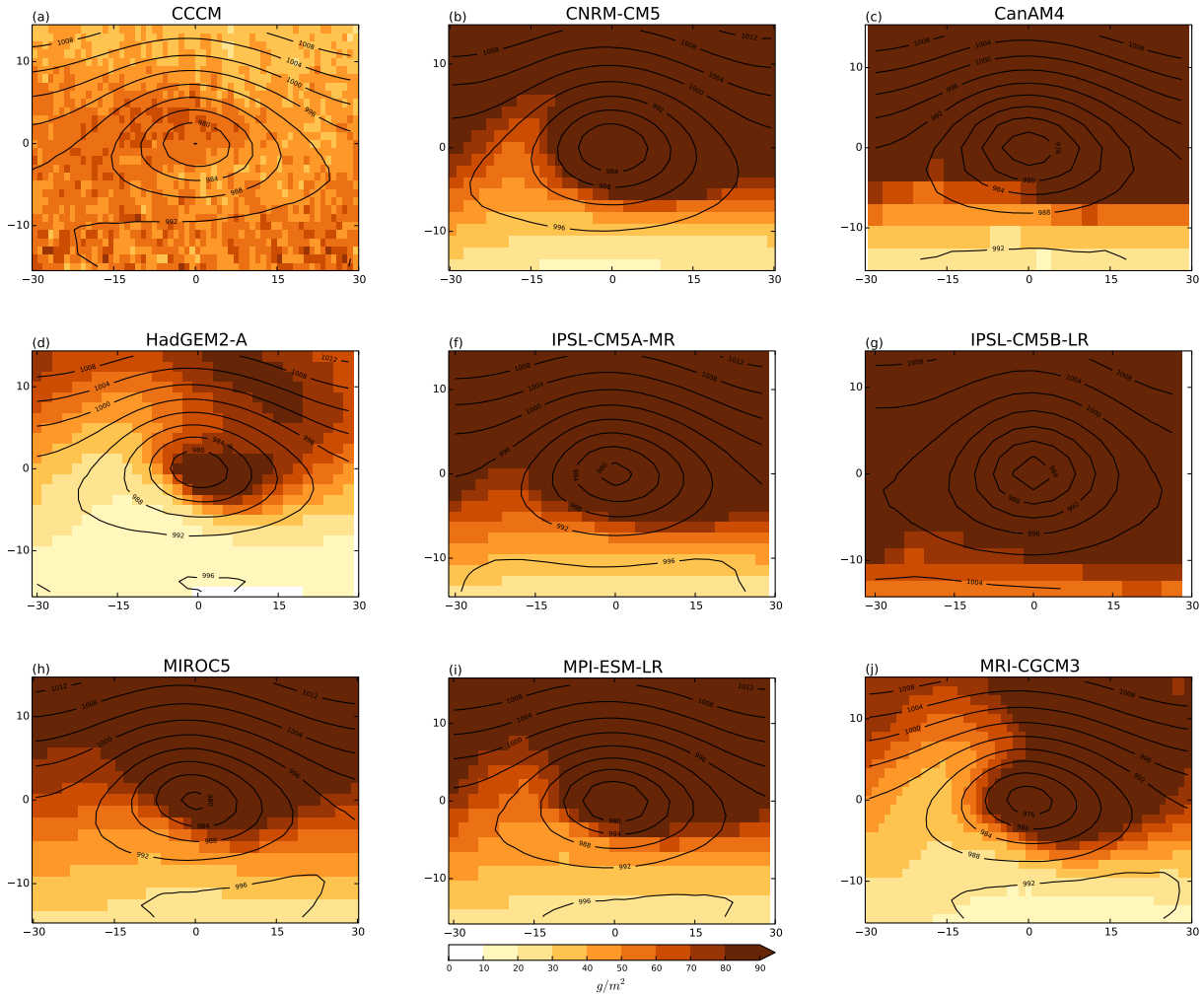


FIG. 8. Liquid water path around cyclone centres over the Southern Ocean in Austral Summer (December-January-February). Cyclone composites calculated using the method of Field and Wood (2007). (a) CCCM data, and (b-j) CMIP5 amip experiment.

### Ice Water Path

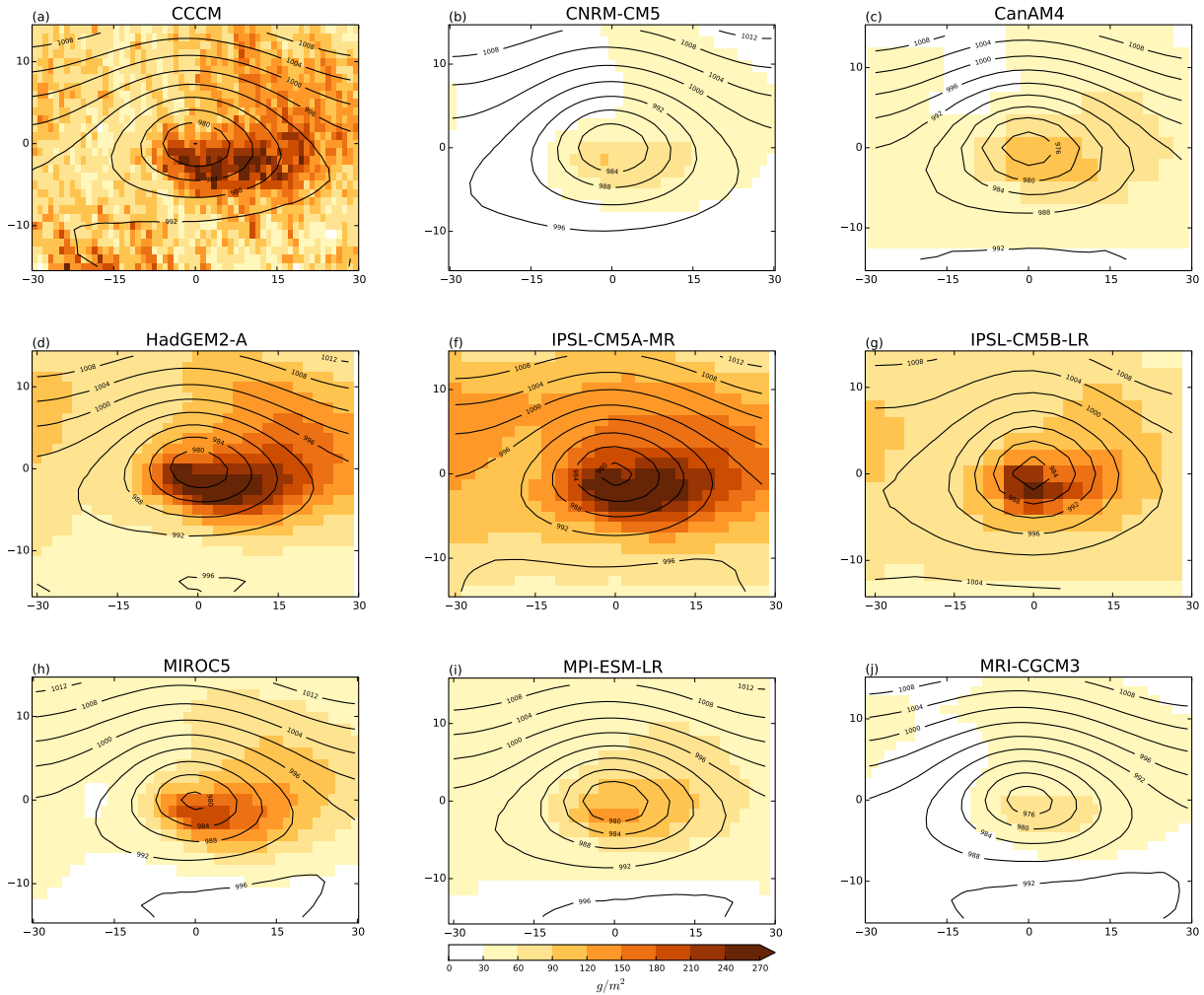


FIG. 9. Ice water path around cyclone centres over the Southern Ocean in Austral Summer (December-January-February). Cyclone composites calculated using the method of Field and Wood (2007). (a) CCCM data, and (b-j) CMIP5 amip experiment.